# Numerical and Experimental Investigation to the Melting Mechanism of Granular Powders for Vitrification by Induction Thermal Plasmas

M. M. HOSSAIN[1], Y. YAO[1], Y. OYAMATSU[1], T. WATANABE [1], F. FUNABIKI[2] and T. YANO[2]
[1]Department of Environmental Chemistry and Engineering
Tokyo Institute of Technology
G1-22, 4259 Nagatsuta, Yokohama 226-8502
JAPAN
[2] Department of Chemistry and Materials Science, Tokyo Institute of Technology
S7-4, 2-12-1 O-okayama, Tokyo 152-8550
JAPAN
http://www.chemenv.titech.ac.jp/watanabe/

*Abstract:* - In this contribution the melting mechanism of granular raw powders in an induction thermal plasma reactor for glass production has been described from both numerical and experimental point of views. Simulation has been performed to predict the flow and temperature fields within the plasma torch for various flow conditions of carrier gas using a 2-dimensional LTE (local thermodynamic equilibrium) model including a metal tube inserted into the torch for powder and carrier gas injection. Simulated results revealed that the higher the flow-rate of carrier gas, the lower the temperature profiles around the centerline of the torch, and the higher the axial plasma velocity. The average particle size of quenched powders became smaller and the softening temperature decreased with higher flow-rate of carrier gas, because of shorter relaxation time and lower temperature respectively. The numerical results well explained the experimental findings and provided a roadmap for the parameter optimization in the melting process.

*Key-Words:* - **Plasma temperature, Granular powder, Carrier flow-rate, Relaxation time, Particle size.**

## 1 Introduction

Thermal plasmas, source of very high enthalpy, high chemical reactivity offer rapid evaporation rate, steep temperature gradients, wide area and high growth rate, and an attractive and chemically nonspecific route for the synthesis of raw powders. Thus, thermal plasma technology has been found extensive industrial applications for material and environmental processes [1-3]. Among various types of thermal plasma reactors [1], radio frequency induction thermal plasma (ITP) reactors offer several advantages such as high purity due to absence of electrode, large volume of plasma for processing, low plasma velocity and wide pressure range. The high temperature of ITP leads to short evaporation time which translates into relatively small torch with high throughput. A good review of the advancements in the applications of plasmas at different stages of glass production has been narrated by Bessmertnyi [4]. Nowadays, it is a burning issue to reduce the energy consumption and the time in melting the granular raw powders for glass production in industrial level. The traditional technologies used for powder melting in glass industries are inefficient, time consuming and not environment friendly. As the usage of glass has been increasing to meet the demand of modern architecture of buildings and automobile industries, thus, it is crucial how to increase the glass production keeping the energy consumption minimum and environment benign atmosphere. In this circumstance, ITP technology offers the distinct advantage of providing essentially one-step processes and short time avoiding the multitude of steps and long time required in melting the raw powders in glass industries.

In this article, the feasibility of melting raw granular powders for vitrification in reactive thermal plasma systems has been demonstrated both numerically and experimentally. We shall discuss about the influence of carrier gas flow-rate on the temperature and flow fields, particle temperature history, particle size distribution and composition of the quenched powders collected at the reaction chamber in an ITP reactor.

## 2 Modeling

The schematic torch geometry is presented in Fig.1. Table 1 summarizes the torch dimensions and

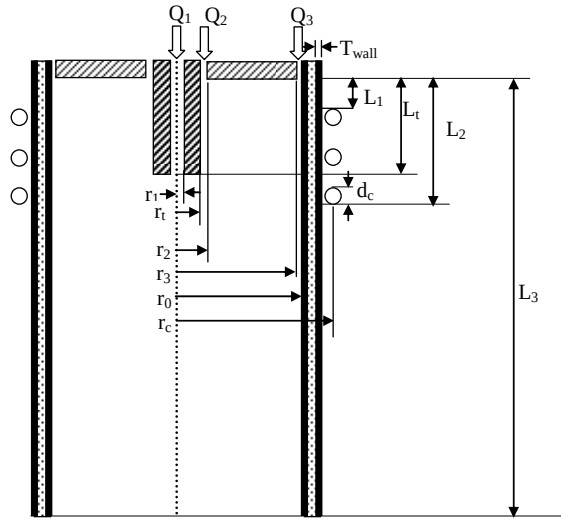


Fig.1 Schematic geometry of ITP torch

operating conditions. The experimental discharge was sustained at 20 kW plug power; assuming 50% overall efficiency, plasma power was set to 10 kW. In this model, the conservation equations along with the vector potential form of Maxwell's equations [5] have been solved simultaneously with some reasonable assumptions and boundary conditions including a metal tube inserted into the plasma torch for carrier gas and powder injection.

## 2.1 Conservation Equations

The following 2-dimensioanl conservation equations have been solved simultaneously along with the vector potential form of Maxwell's electromagnetic equations.

Continuity Equation:

$$\nabla \cdot (\rho \boldsymbol{u}) = 0 \qquad (1)$$

Momentum Equation:

*Axial momentum:*

$$\rho \boldsymbol{u} \cdot \nabla u = -\frac{\partial p}{\partial z} + \nabla \cdot \mu \nabla u + \frac{1}{r}\frac{\partial}{\partial r}\left( r\mu \frac{\partial v}{\partial z} \right) + \frac{\partial}{\partial z}\left( \mu \frac{\partial u}{\partial z} \right) + F_z \qquad (2)$$

*Radia momentum:l*

$$\rho \boldsymbol{u} \cdot \nabla v = -\frac{\partial p}{\partial r} + \nabla \cdot \mu \nabla v + \frac{1}{r}\frac{\partial}{\partial r}\left( \mu r \frac{\partial v}{\partial r} \right) + \frac{\partial}{\partial z}\left( \mu \frac{\partial u}{\partial r} \right) - \frac{2\mu v}{r^2} + \rho \frac{w^2}{r} + F_r \qquad (3)$$

*Theta momentum:*

$$\rho \boldsymbol{u} \cdot \nabla w = \nabla \cdot \mu \nabla w - \frac{\rho v w}{r} - \frac{1}{r}\frac{\partial (\mu w)}{\partial r} + \mu \frac{\partial}{\partial r}\left( \frac{w}{r} \right) \qquad (4)$$

Energy Equation:

$$\rho \boldsymbol{u} \cdot \nabla h = \nabla \cdot \left( \frac{\kappa}{C_p} \nabla h \right) + \overset{\circ}{P} - \overset{\circ}{R} \qquad (5)$$

Maxwell's Equation:

$$\frac{\partial^2 \boldsymbol{A}_\theta}{\partial z^2} + \frac{1}{r}\frac{\partial}{\partial r}\left( r \frac{\partial \boldsymbol{A}_\theta}{\partial r} \right) - \frac{\boldsymbol{A}_\theta}{r^2} = j\mu_0 \sigma \omega \boldsymbol{A}_\theta \qquad (6)$$

Source Terms:

$$F_r = \frac{1}{2}\mu_0 \sigma \,\mathrm{Real}\left[ \boldsymbol{E}_\theta \boldsymbol{H}_z^* \right]$$

$$F_z = \frac{1}{2}\mu_0 \sigma \,\mathrm{Real}\left[ \boldsymbol{E}_\theta \boldsymbol{H}_r^* \right]$$

$$\overset{\circ}{P} = \frac{1}{2}\sigma \left[ \boldsymbol{E}_\theta \boldsymbol{E}_\theta^* \right]$$

$$\overset{\circ}{R} = \text{Volumetric radiation loss}$$

Where, $\nabla$: gradient operator in cylindrical coordinates, $\rho$: mass density, $\sigma$: electrical conductivity, $\kappa$: thermal conductivity, $C_p$: specific heat at constant pressure, $\boldsymbol{u}$: velocity vector, $\boldsymbol{A}_\theta$: vector potential, $h$: enthalpy, $\boldsymbol{E}_\theta$: electric field, $\boldsymbol{H}$: magnetic field, $\mu$: viscosity, $\omega$: angular frequency ($2\pi f$), $\mu_0$: permeability of free space ($4\pi \times 10^{-7}$ H/m), $j$: complex vector ($\sqrt{-1}$).

## 2.2 Assumptions

The present computation was concerned only within the torch. The discharge was supposed to be sustained in a cylindrical water-cooled quartz tube with argon as carrier gas injected through a nozzle tube, plasma gas, and sheath gas with a swirl to stabilize the plasma and protect the quartz tube from overheating. It was assumed that plasma flow was steady, 2-dimensional, axi-symmetric, laminar and incompressible. The plasma was in the state of LTE and optically thin. Furthermore, viscous dissipation and displacement currents were negligible and each coil turn was assumed to be planner.

Table 1: Torch dimensions & operating conditions

| | |
|---|---|
| Torch length ($L_3$) | 190 mm |
| Distance to initial coil position ($L_1$) | 19 mm |
| Distance to end of coil position ($L_2$) | 65 mm |
| Length of injection tube ($L_t$) | 52 mm |
| Coil diameter ($d_c$) | 5 mm |
| Wall thickness of quartz tube ($T_{wall}$) | 1.5 mm |
| Torch radius ($r_0$) | 22.5 mm |
| Coil radius ($r_c$) | 32 mm |
| Inner radius of injection tube ($r_1$) | 1 mm |
| Outer radius of injection tube ($r_t$) | 4.5 mm |
| Outer radius of inner slot ($r_2$) | 6.5 mm |
| Inner radius of outer slot ($r_3$) | 21.5 mm |
| Plug power | 20 kW |
| Plasma power | 10 kW |
| Working frequency | 4 MHz |
| Working pressure | 101.3 kPa |
| Flow rate of carrier gas ($Q_1$) | 3 ~ 9 l/min of Argon |
| Flow rate of plasma gas ($Q_2$) | 3 l/min of Argon |
| Flow rate of sheath gas ($Q_3$) | 30 l/min Argon |

### 2.3 Boundary Conditions

The boundary conditions for conservation equations of mass, momentum, and energy were: at the inlet, gas temperature was set to 300 K and uniform velocity profiles were assumed based on the given flow rates; on the axis of symmetry, the symmetry conditions were imposed; on the walls, the no-slip condition was assumed; the outer wall temperature was set to 350 K; and, at the exit, axial gradients were set equal to zero. The inserted tube was assumed water cooled at 300 K and the velocity on the tube wall was set to zero.

### 2.4 Computational Procedure and Thermophysical Properties

The governing equations, which are listed in previous section, were solved numerically using the SIMPLER algorithm of Patankar [6]. The algorithm was based on a control-volume finite-difference scheme for solving the transport equations of incompressible fluids. Calculations were performed for a 42 (in radial direction) by 87 (in axial direction) non-uniform grid system.

Thermodynamic and transport properties of argon gas required for simulation included mass density, specific heat at constant pressure, viscosity, electrical and thermal conductivity and radiative loss coefficient. The transport properties, which are function of temperature, were calculated under LTE conditions using Chapman-Enskog first approximation to Boltzmann equation [7].

### 2.5 Simulated Results and Discussion

Simulation has been performed for the torch shown in Fig.1 and the operating conditions described in Table 1 to investigate the carrier gas flow-rate effect on temperature and velocity fields. Fig.2 depicts the

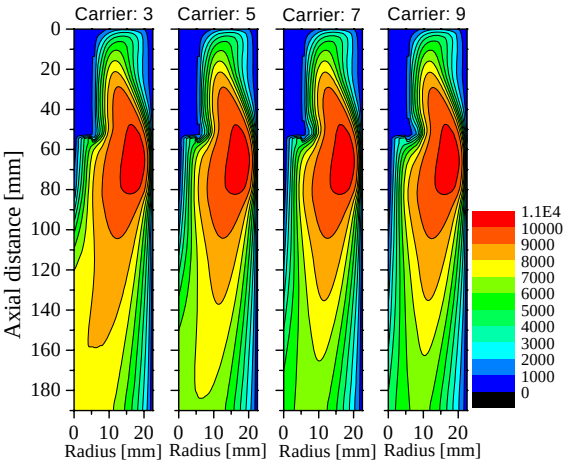


Fig.2 Effects of carrier gas flow-rate on the temperature contours.

predicted temperature contour within the torch. It is observed that at increased carrier flow-rate, the temperature sharply decreases along the centerline and also the high temperature zones shrink. This is attributed from the large heat transfer to the cold carrier gas injected through the inserted nozzle tube. The high temperature (6000 K to 11000 K) is sufficient enough to melt the injected granular powders in the torch within very short time. Fig.3 shows the plasma temperature along the centerline for different carrier gas flow-rate. It is found that plasma temperature increases with the distance from the nozzle exit, attains the maximum value and again decreases at the torch exit for smaller carrier flow-rate. It is evident that carrier gas flow-rate strongly affects the temperature around the centerline of the torch. Fig.4 reveals that the axial plasma velocity along the centerline increases with carrier flow-rate because of large momentum of carrier gas. Maximum velocity is attained below the coil region due to the effect of Lorentz force. Due to the increased momentum, the large carrier gas flow-rate in turn, enhances the flow of melted powders to deposit on the substrate.

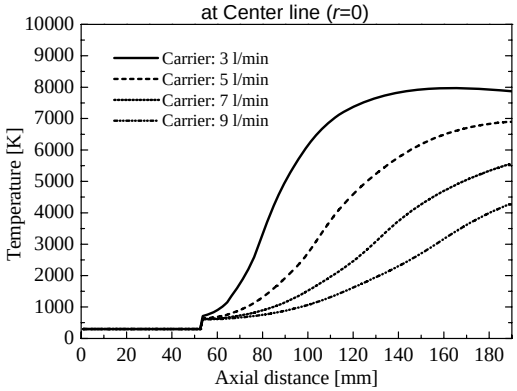


Fig.3 Impact of carrier gas flow-rate on the centerline ($r$ = 0) temperature.

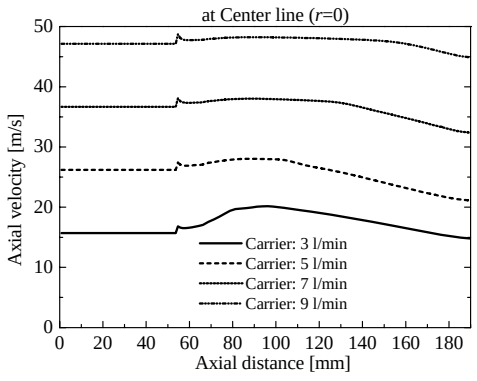


Fig.4 Impact of carrier gas flow-rate on the axial plasma velocity at the centerline ($r$ = 0).

## 3 Particle Temperature

Using the temperature profiles presented in the previous section, the particle temperature with distance from the nozzle tube was predicted by solving the equation of energy balance considering heat transfer due to plasma flow. For a spherical particle with symmetric boundary conditions, the heat transfer into the particle is described by the conduction equation, i.e.,

$$\rho C_{pw} \frac{\partial T}{\partial t} = \frac{1}{r^2} \frac{\partial}{\partial r} \left( r^2 \kappa \frac{\partial T}{\partial r} \right) \quad (7)$$

According to Lee *et al* [8], the Nusselt number correlation for heat transfer between plasma and particles can be expressed as:

$$\mathrm{N_u} = \left(2 + 0.6\,\mathrm{Re}^{1/2}\,\mathrm{Pr}^{1/3}\right) \left( \frac{\rho_\infty \mu_\infty}{\rho_w \mu_w} \right)^{0.6} \left( \frac{C_{p\infty}}{C_{pw}} \right)^{0.38} \quad (8)$$

Where, *r:* radial distance from the center of the particle, *k:* Boltzmann's constant, Re: Reynolds number, Pr: Prandtl number, and $\rho$, $C_{pw}$ and $\kappa$ are the density, specific heat, and thermal conductivity of the particle respectively.

Using the boundary conditions described in Ref. [8], the particle temperature was calculated with the distance from the nozzle exit. The particle diameter, vaporization temperature and vitrification

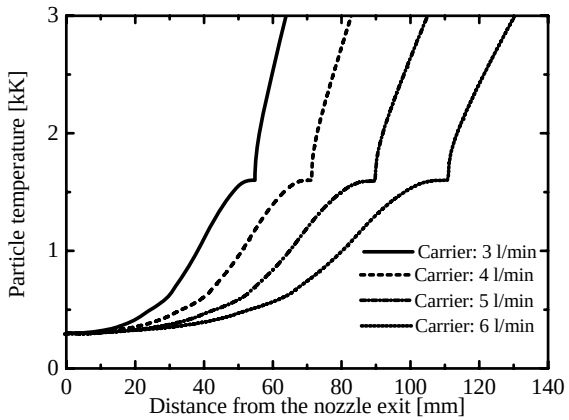


Fig.5 Particle temperature profiles with the distance from the nozzle exit

temperature were set to 58 $\mu$m, 2500 K and 1672 K respectively. The mass density, effective thermal conductivity and specific heat of the feed powders are 2300 kg/m$^3$, 0.1 W/m-K and 2200 J/kg-K respectively. The void fraction was set to 80%. As the powder is melted and evaporated, particle's axial velocity reaches very close to plasma velocity. The particle temperature with distance from the nozzle exit is shown in Fig.5 for different carrier gas flow-rate. It is evident that close to the nozzle exit, carrier flow-rate has no strong effect; however, with the distance from the nozzle exit, larger carrier gas flow-rate reduces the heat transfer to the particles.

# 4 Experimental

## 4.1 Setup and Measurement Details

The experimental setup consists of a power supply unit (4 MHz, 20 kW), an induction plasma torch, and an attached reaction chamber below the torch. The plasma torch consists of a water-cooled quartz tube (45 mm inner diameter and 190 mm length), surrounded by a water-cooled three-turn induction coil which couples electromagnetic (EM) energy to the plasma at a frequency of 4.0 MHz. The plug power was 20 kW. Argon gas was introduced as the carrier gas (2.5 to 6.5 l/min), the plasma supporting gas (3 l/min), and the sheath gas (30 l/min). The sheath gas, injected with an induced swirling motion from the outer slots, protected the inner surface of the quartz tube from overheating.

The granular powders of raw material were prepared by the spray-drying method from the reagents of $Na_2CO_3$, $CaCO_3$ and $SiO_2$ for the soda-lime-silica glass with the composition of $Na_2O$:16, CaO:10 and $SiO_2$:74 in wt%. $Na_2O$ mainly reduces the melting temperature of raw powders. The raw materials with about 58 μm in diameter was injected into the thermal plasma at a rate of 5 g/min by powder feeder and melted glass powders were collected on a water-cooled substrate at 340 mm down to the nozzle. Other experimental conditions are listed in Table 1.

The micrograph and size distribution of the particles was carried out by scanning electron microscope (SEM) on JSM5310 (JEOL). The structures of the collected powders were determined by X-ray diffractometry (XRD). XRD was carried out on Miniflex (Rigaku) with Cu $K_\alpha$ radiation at 30 kV and 15 mA. The data were collected in the 2θ range 3-90° with a step size of 0.02° and a scan speed of 4°/min. The thermogravimetric differential thermal analysis (TG-DTA), for thermal analysis was performed with thermogravimetry on TG8120 (Rigaku); the measured temperature in the range of 20-1400°C, at the rate of 10°C/min. The composition of the powders was analyzed by ICP-8100 (SHINADZU).

## 4.2 Experimental Results

Fig.6 depicts the carrier gas flow-rate effect on the particle size and collecting ratio of quenched soda lime powder. It was found that the average particle size has a decreasing tendency with carrier gas flow-rate. The high flow-rate of carrier gas increased the axial plasma and particle velocity which, in turn, decreased the relaxation/residence time. Thus, one of the probable reasons was that under high heating rate, the melted powder structure did not have sufficient relaxation time and the compounds constituting the melted glass decompose, which was

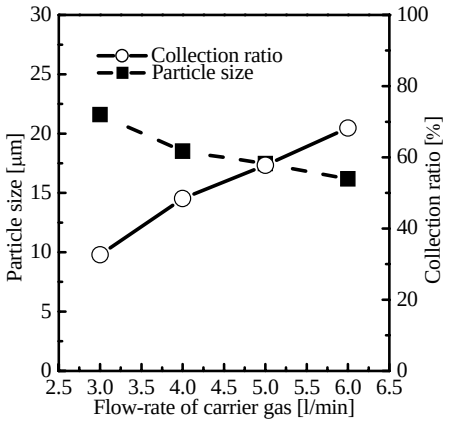


Fig.6 Effects of carrier gas flow-rate on the particle size distributions and collection ratio.

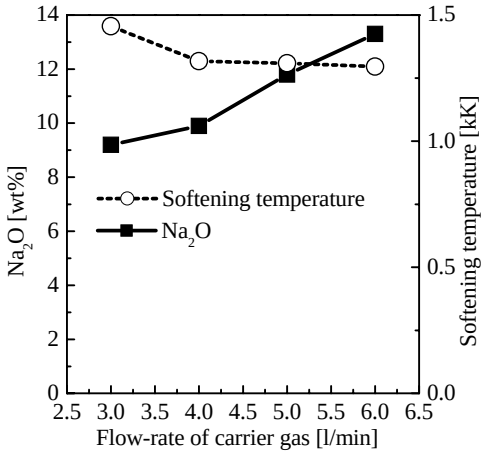


Fig.7 Distributions of Softening temperature and $Na_2O$ contents of the quenched powders with the flow-rate of carrier gas.

accompanied by the formation of smaller particle size [4]. Moreover, the high momentum caused by the higher carrier flow-rate, enhanced the flow of smaller particles towards the substrate. Thus, the collection ratio became larger with carrier flow-rate. Fig.7 describes the effects of carrier gas flow-rate on the softening temperature and content of $Na_2O$ in the quenched powders. The lower plasma temperature and shorter relaxation time, caused by the larger carrier flow-rate, resulted the lower evaporation rate of $Na_2O$, which in turn gave rise to the composition of $Na_2O$ in the quenched powder. The increase of composition of $Na_2O$ in the quenched powder indicates the smaller heat transfer to the particles at larger flow-rate of carrier gas. Thus, the softening temperature, which was affected by the composition of $Na_2O$ in the powders, decreased at higher carrier gas flow-rate. These experimental finds are consistent with the theoretical predictions described in Fig.5.

## 5 Conclusions

A 2-dimensional LTE model was used to simulate the temperature and velocity profiles including a metal tube inserted into the plasma torch for injecting the carrier gas and granular raw powders. It was found that higher carrier gas flow-rate caused to decrease the temperature and increase the velocity profiles around the centerline of the torch, which in turn, affected the quenched particle size distribution, composition of quenched powders and throughput. Experimental analysis showed that at increased carrier gas flow-rate, the average particle size and softening temperature decreased, whereas collection ratio increased. Larger carrier gas flow-rate also reduced the heat transfer to the particles. The simulated results well explained the experimental findings and were consistent with those. Even if, we did not consider the effects of the particle loading on the temperature and velocity profiles that will be the subject of the future work.

*Acknowledgements*

The financial support provided by Strategic Development of Energy Conservation Technology Project of NEDO (New Energy and Industrial Technology Development Organization, Japan) is gratefully acknowledged.

*References:*

[1] R. M. Young and E. Pfender, "Generation and Behavior of Fine Particles in Thermal Plasmas-A Review," *Plasma Chem .Plasma Process.*, vol. 5, 1985, pp.1-37.

[2] M. Sakano, M. Tanaka and T. Watanabe, "Application of radio-frequency thermal plasmas to treatment of fly ash," *Thin Solid Films*, vol. 386, 2001, pp.189-194.

[3] X. H. Wang, K. Eguchi, C. Iwamoto and T. Yoshida, "Ultrafast thermal plasma physical vapor deposition of thick films," *Sci. Technol. Adv. Materials*, vol. 4, 2003, pp. 159-165.

[4] V.S. Bessmertnyi, "Plasma Treatment of Glasses (A Review)," *Glass and Ceramics*, vol. 58, 2001, 121-124.

[5] J. Mostaghimi, K. C. Paul and T. Sakuta, "Transient response of the radio frequency inductively coupled plasma to a sudden change in power," *J. Appl. Phys.*, vol. 83, 1998, pp. 1898-1908.

[6] S. V. Patankar, *Numerical Fluid Flow and Heat Transfer*, Hemisphere, New York, 1980.

[7] Y. Tanaka, K. C. Paul and T. Sakuta, "Thermodynamic and Transport Properties of $N_2/O_2$ Mixtures at Different Admixture Ratio," *Trans. IEE Japan*, vol. 120-B, 2000, pp. 24-30.

[8] L. C. Lee, Y. P. Chyou and E. Pfender, "Particle Dynamics and Heat and Mass in Thermal Plasmas. Part II. Particle Heat and Mass in Thermal Plasmas," *Plasma Chem. Plasma Process.* vol. 5, 1985, pp. 391-414.